Dynamic hazard zone modeling for proximity detection in work zones

Ayenew Yihune Demeke, Youjin Jang, Inbae Jeong
Automation in Construction, 190, 107132 (2026)

The published version (version of record) is available at: https://doi.org/10.1016/j.autcon.2026.107132

This is the author's accepted manuscript. The final published version is available at: 10.1016/j.autcon.2026.107132

Dynamic Hazard Zone Modeling for Proximity Detection in Work Zones

Ayenew Yihune Demeke[1], Youjin Jang, Ph.D.[2], and Inbae Jeong, Ph.D.[3]

[1] Dept. of Civil, Construction and Environmental Engineering, North Dakota State Univ., Fargo, ND 58108, USA; Email: ayenew.demeke@ndsu.edu

[2] Dept. of Civil, Construction and Environmental Engineering, North Dakota State Univ., Fargo, ND 58108, USA; Email: y.jang@ndsu.edu

[3] Dept. of Mechanical Engineering, North Dakota State Univ., Fargo, ND 58108, USA; Email: inbae.jeong@ndsu.edu (corresponding author)

Abstract

Construction work zones are among the most hazardous environments due to the close interaction between workers and moving equipment. Existing proximity detection systems often rely on static geometric hazard zones that fail to adapt to real-time equipment dynamics, leading to false alarms or missed detections. This paper presents a dynamic probabilistic hazard zone model that continuously adjusts its size and orientation based on real-time kinematic data from sensors mounted on construction equipment. The model represents risk as a continuous spatial probability field using a bivariate generalized Gaussian distribution, enabling adaptive and multi-level hazard boundaries. Simulation and field experiments were conducted to evaluate the model's performance against a conventional static circular hazard zone. Results show that the proposed model significantly reduces false positives while maintaining stable detection across varying speeds. These findings suggest that the dynamic hazard zone model has the potential to improve safety management across diverse construction work zone environments, provided that broader validation across additional equipment types and field conditions is undertaken.

Key words

Dynamic hazard zoning, proximity detection, construction zone, worker safety

1. Introduction

Construction sites remain hazardous environments where the dynamic interplay between construction equipment and workers, and concurrent operations poses persistent safety risks. The combination of constrained working spaces, simultaneous tasks, and continuous movement of heavy machinery creates an environment prone to accidents, including collisions between construction equipment and workers on foot. Despite advancements in proximity detection systems, recent crash-risk analyses [1,2] and reviews of sensor-based systems for collision prevention [3] show that such collisions and near-miss incidents continue to account for significant injuries and project delays, underscoring the need for more effective safety frameworks.

Effective prevention of collisions and near-miss incidents between construction equipment and workers on foot hinges on the precise modeling of hazard zones. Such zones must enable timely detection of potential risks to ensure adequate response time for both workers and operators, while maintaining sufficient accuracy to minimize false alarms that could undermine the credibility of the system and lead to desensitization [4,5]. A range of hazard zoning approaches has been proposed in both practice and scholarly literature, each offering distinct benefits while presenting inherent limitations.

Many existing hazard zone models rely on fixed geometric boundaries around equipment, with predefined safety zones used to support proximity detection and worker warning [6,7]. Field evaluations of such predefined zones demonstrate their practical value for communicating hazards, but the resulting boundaries remain limited because they do not adapt to the real-time movements of construction machinery [8]. This limitation often results in either insufficient protection or excessive false alerts, reducing the reliability of current systems [4,6]. Zones large enough to account for high-speed motion often result in frequent false alarms when equipment is stationary or moving slowly, while zones sized conservatively may fail to provide adequate warning when speeds increase. Several studies have attempted to address this by tailoring hazard zone dimensions to typical equipment characteristics, such as equipment shape and braking distance [9] or representative operating speeds [4,10]. However, these models remain effectively static, as they do not incorporate real-time kinematic data such as continuously changing speed and heading. As a result, current systems often exhibit limited responsiveness and generate false alerts, particularly in dynamic and space-constrained environments such as active construction sites [3].

Furthermore, existing models typically define a single hazard zone around construction equipment, where workers receive an immediate hazard alarm without any prior warning. This approach can be inconvenient, as it triggers a sudden alert, requiring workers to react without preparation. Implementing a multi-level hazard zone would provide progressive warnings, allowing workers to receive early cautions as they approach a potentially hazardous area [7], [8].

Taken together, existing approaches remain largely geometric rather than kinematic, treat risk primarily as a binary inside-or-outside condition, and lack a unified mathematical formulation that adapts to equipment motion while representing multiple levels of risk. Despite prior efforts, real-time hazard zone formulations that incorporate equipment kinematics and express risk as a graded, multi-level spatial quantity remain underdeveloped.

To address this limitation, this study develops a dynamic probabilistic hazard zone model grounded in the bivariate generalized Gaussian distribution. The proposed model uses equipment kinematics measured by RTK GNSS and IMU sensors, while worker presence is captured through wearable devices equipped with the same sensing technologies. By translating continuously measured equipment motion into adaptive spatial risk fields, the model generates multi-level hazard boundaries that vary according to the direction and magnitude of equipment movement. The bivariate generalized Gaussian distribution is adopted as the modeling primitive because it represents risk as a continuous spatial field, produces elliptical and superelliptical contours that align naturally with the longitudinal direction of equipment motion, and provides a tunable shape parameter for reflecting observed hazard distributions. While worker localization is incorporated for proximity assessment, the modeling framework is developed primarily from the equipment side. The proposed model is evaluated through simulation and field experiments and compared with a conventional static circular baseline to assess its ability to reduce false alarms while preserving true hazard detection. The main contribution of this work is therefore a unified probabilistic framework that translates continuously measured equipment kinematics into adaptive, multi-level hazard boundaries, supported by quantitative evidence from both simulation and field testing that the framework reduces false alarms relative to a static baseline while preserving detection of true hazards.

This paper is structured as follows. The next section reviews prior works in hazard zone modeling and proximity detection. The methodology, including model development and hazard zone dimension optimization, is presented thereafter, with the experimental design and evaluation metrics described subsequently. This is followed by the results of the field experiments and comparative analysis. The subsequent section discusses key findings, limitations, and implications for real-world deployment. Finally, the paper concludes with a summary of contributions and directions for future research.

2. Literature Review

Prior research on hazard zone modeling and proximity detection in construction environments is reviewed in this section. The discussion begins with conventional static hazard zoning approaches, followed by multi-level zoning strategies and probabilistic risk modeling. Advances in real-time sensing and communication technologies that enable adaptive hazard zone implementation are also examined.

2.1. Hazard Zone Modeling Approaches

Early approaches to hazard zone mapping typically employ static models using fixed-size geometric shapes (often circles) to denote danger areas around equipment. For instance, Wang and Razavi [6] proposed circular hazard and warning zones around construction equipment, where breaching an outer warning zone triggers an alert and entering the inner hazard zone indicates imminent danger. Similarly, prior work has used predefined circular or rectangular zones for excavator warning and control [7], worker response to proximity warnings [8], and radio frequency (RF)-based autonomous worker-equipment alerting [13]. These static zones are simple and intuitive; however, they assume a one-size-fits-all radius that does not change with the equipment's state. A static circle offers the same hazard area whether a machine is idle or moving at high speed.

This leads to two major issues: (1) If the zone is sized for worst-case (high speed), a slow or stationary machine will cause unnecessary alarms, reducing system credibility [10]. (2) If sized smaller to avoid false alarms, a fast-moving machine may outpace the hazard zone, yielding insufficient warning distance [14]. In addition, the shape of hazard zones affects their effectiveness, as different equipment types have unique geometries and movement patterns that require tailored zone shapes to accurately reflect risk areas. Shen et al. [9] underscored these limitations and proposed a standardized procedure for tailoring hazard zone shape and size to specific equipment types. Their method used typical equipment speed and braking distance to define custom zone dimensions, improving realism over one-size static zones. Yet, because typical values were used in lieu of real-time data, even these tailored static zones could not fully address dynamic conditions on site. In congested environments common to many construction sites, static thresholds often misidentify safe situations as hazards and vice versa [3]. As Awolusi and Marks [15] note, active work zone safety systems require more responsive sensing technologies to prevent accidents. Park et al. [12] affirmed that previous research insufficiently explored how different factors, such as equipment type, speed, and movement patterns, affect proximity sensing. Their study, which improved dynamic proximity sensing for smart work zones, emphasized that a "one-size-fits-all" hazard boundary is inadequate and recommended defining hazard zones that adapt in real time to equipment behavior. Overall, the literature clearly points toward the need for adaptive hazard zoning that can expand or contract based on operational conditions, rather than remaining static.

One important consideration in hazard zoning is providing multi-level hazard zones instead of a single binary boundary. Many early systems only define a single threshold: workers are either "inside" or "outside" the danger zone [4,7]. In contrast, multi-tiered approaches establish gradations such as caution, warning, and danger zones, which correspond to increasing risk levels [13]. Teizer et al. [11] conducted a field-test with a three-level zoning system ("warn," "slow," "stop") using a magnetic field–based proximity detection technology. In their setup, workers wore sensors that detected magnetic fields emitted by equipment; entering the outer field triggered a warning, closer proximity triggered machinery slow-down, and breaching the innermost zone signaled an emergency stop. This layered approach provides earlier alerts for emerging hazards and only escalates to severe alarms when absolutely necessary, helping minimize unnecessary interruptions. Luo et al. [8] also studied how workers respond to tiered safety zones in a field experiment, finding that workers were more likely to heed early warnings that preceded the critical hazard zone. By distinguishing moderate vs. critical risk, multi-level models add nuance to hazard communication, which can improve compliance and reduce alarm fatigue. However, implementing multiple zones requires careful calibration to ensure each threshold is meaningful and actionable, a topic that still sees ongoing research [11,13].

Probabilistic and uncertainty-aware methods have become more common in construction safety and related infrastructure research to represent uncertain hazard conditions and support risk assessment. Prior studies have applied fuzzy probabilistic frameworks to occupational hazard assessment [16] and construction-project risk evaluation under uncertainty [17], while related infrastructure modeling work has demonstrated the value of probabilistic uncertainty quantification for systems with uncertain inputs and parameters [18]. Rather than using deterministic thresholds, these methods characterize safety risk as a continuous field, capturing uncertainties in worker behavior, hazard dynamics, and environmental conditions. In the broader construction safety domain, researchers have applied probabilistic methods to improve risk estimation. Park et al. [19] developed a sensor-based safety risk assessment model using probabilistic evaluation to quantify a worker's exposure to moving hazards. Zhang et al. [20] utilized stochastic processes to model safety risks on construction sites, demonstrating that probability-driven models can better predict accidents under uncertainty. Abdrakhmanova [21] et al. proposed a probabilistic hazard analysis framework for industrial operations with dynamically changing exposure zones. These studies illustrate that risk is not binary and exists along a continuum from safe to dangerous conditions, which can be mathematically modeled. However, they do not directly address the spatial modeling of hazard zones in real time, particularly in relation to moving construction equipment in dynamic work environments.

2.2. Real-Time Sensing and Hazard Zone Implementation

Implementing adaptive hazard zones in practice requires robust real-time tracking and sensing of equipment and workers. Recent technological advances in real-time location systems (RTLS) and the Internet of Things (IoT) have greatly enhanced the feasibility of dynamic hazard monitoring on construction sites. Several studies and proposed systems for construction work zones have demonstrated the use of technologies such as GNSS, IMUs, Ultra-Wideband (UWB) radios, Bluetooth beacons, and RFID tags to continuously track the positions and movements of equipment and workers in real time, ranging from UWB locating systems developed for worker safety [22,23] to remote-sensing platforms for automated jobsite data acquisition [24]. These systems provide the high-frequency data needed to update hazard zones on the fly, reflecting current site conditions. For example, Umer and Siddiqui [23] demonstrated the use of a UWB RTLS on jobsites, showing it can reliably locate resources within decimeter accuracy and thus serve as a backbone for proximity detection. Soltanmohammadlou et al. [25] reviewed applications of RTLS in construction safety and concluded that such technologies markedly improve situational awareness in dynamic environments. As a result, integrating RTLS with proximity detection systems has become a focal point in recent construction safety research.

Several sensor-based proximity alert systems have been prototyped with promising results [26]. Kim et al. [27] developed an IoT-based proximity safety system using wearable Personal Protection Units (PPUs) for workers and Equipment Protection Units (EPUs) on machines, communicating via Bluetooth Low Energy (BLE). Their system uses signal processing (particle filtering of RSSI signals) to estimate distances, and triggers tiered audio/vibration alerts to both workers and operators as thresholds are breached. In a related vein, Ciribini et al. [28] introduced a low-cost UWB-based proximity warning system designed for flexible deployment on resource-constrained job sites. Their system can operate with or without fixed UWB anchors, using direct ranging between tags on workers and equipment to detect dangerous proximity.

Building on recent advancements in sensing technologies, data from IoT devices can now be harnessed to create truly adaptive hazard zones that respond in real time. Data from sensor devices such as GNSS, IMU, UWB, and RFID enable continuous calculation of equipment speed, acceleration, and trajectory, which can feed into dynamic zone models. These technologies have been successfully tested in active construction environments in various setups, demonstrating improvements in safety outcomes [23].

Additionally, advancements in real-time wireless communication and mesh networking areas enable an easy implementation of adaptive hazard zones in large-scale or distributed construction sites using efficient and low power communication mechanisms. Long-range communication methods like LoRaWAN have been explored to transmit hazard warnings over large sites or highway stretches. Teizer et al. [29], for example, showed that LoRaWAN could track construction resources across a wide area with low power consumption, supporting site-wide safety monitoring. Recent work by Younesi Heravi et al. [30] and Jeong et al. [31] on smart construction monitoring systems suggests that an interconnected network of sensors and edge AI can greatly improve the responsiveness and accuracy of safety interventions on site. The introduction of edge computing and digital twins also presents new opportunities: edge computing can support real-time data processing and timely system updates [32], while digital twin applications in transportation infrastructure show how field conditions can be represented in virtual environments for monitoring and decision support [33,34]. In this context, wearable and onboard sensors can stream data to edge devices or a digital twin of the construction zone, where hazard zones are updated in a virtual model in real time and alerts are pushed to workers' devices. This allows safety managers to visualize evolving risk zones on a dashboard and intervene as needed.

These studies generally show that advancements in sensor devices and their utilization for RTLS applications in construction sites are critical enablers for implementing dynamic hazard zones that adapt to different parameters based on kinematic information collected from sensors installed on construction equipment. Furthermore, the findings suggest that once dynamic hazard zone models are developed, they can be effectively deployed in real-world environments through the use of mesh networks and related communication technologies, allowing for continuous tracking of worker proximity and comprehensive site monitoring.

In summary, while various approaches have been proposed for proximity detection and hazard zone modeling, many rely on static or semi-adaptive boundaries that fail to account for real-time equipment dynamics. Probabilistic methods have been explored in broader safety risk contexts, but their application to spatial hazard zoning around moving construction equipment remains limited. This study addresses these gaps by developing and validating a dynamic hazard zone model that employs a probabilistic spatial representation to capture continuous risk gradients and multi-level boundaries, continuously adapting to real-time equipment kinematics, with the aim of improving detection accuracy and reducing false alarms, thereby enhancing operational reliability in diverse construction environments.

3. Methodology

This section describes the development and refinement of the proposed dynamic hazard zone model. The probabilistic framework underlying the model is first introduced, followed by the derivation of hazard zone dimensions from equipment geometry and motion characteristics. The section then presents the simulation-based optimization process that leads to the generalized Gaussian representation used for final implementation. An overview of the full workflow, from sensor input through hazard zone generation to evaluation, is provided in Fig. 1, and the components of this workflow are described in detail in the subsequent subsections.

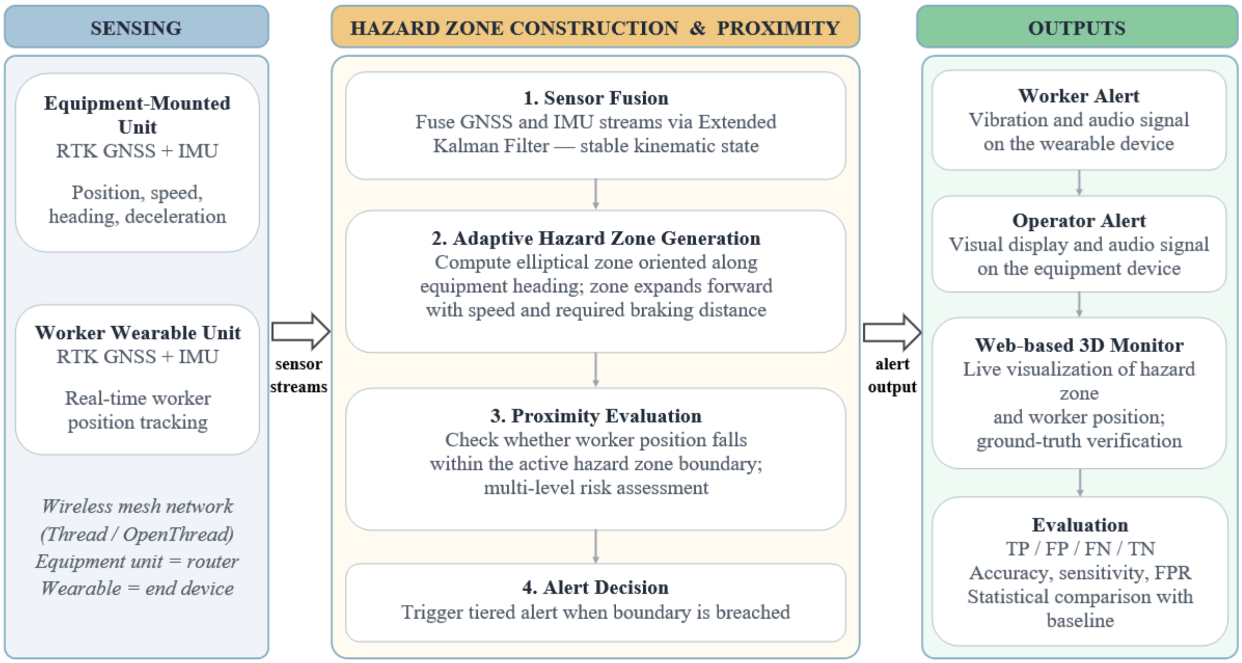

Fig. 1. Overall workflow of the proposed method

3.1. Model Development

This study formulates a probabilistic hazard zone model in which the risk of collision is represented as a continuous spatial probability field around the equipment. The model employs a bivariate Gaussian distribution whose probability density function is given in Eq. (1). In this formulation, the joint density f(x, y) assigns a probability value to every spatial location relative to the equipment center, with higher values indicating greater collision risk. This representation naturally produces elliptical iso-probability contours whose shape, size, and orientation can be controlled through the distribution parameters. The model leverages high-precision RTK GNSS and IMU data to continuously update these parameters based on the equipment's real-time speed and heading, enabling the hazard boundary to adapt dynamically to changing motion conditions.

The bivariate Gaussian distribution is adopted in this work for several reasons. It represents risk as a continuous spatial field rather than a binary inside-or-outside region, which is consistent with the empirical observation that proximity-related risk decays smoothly with distance from the equipment rather than terminating at a hard boundary. Its level sets are ellipses whose principal axes can be aligned with the longitudinal and lateral directions of equipment motion, giving a natural correspondence between the geometry of the distribution and the geometry of the hazard. In addition, isolines of the distribution corresponding to different probability thresholds can be used to define multiple hazard tiers, such as caution, warning, and danger, from a single underlying parameterization. As shown later in Section 3.2, the standard Gaussian formulation is subsequently generalized to a bivariate generalized Gaussian to better match the spatial distribution of hazard events observed in simulation, while preserving these properties.

The formulation developed in this section is intended for construction equipment whose hazard footprint is dominated by translational motion along a primary heading direction, such as haul trucks, rollers, and similar vehicles commonly encountered in construction work zones. Equipment classes with substantially different kinematic signatures, including rotating cranes, articulated boom equipment, and concrete pump trucks, would require additional terms to capture motion components such as swing radius or boom reach, and are not modeled here.

A series of elliptical projections with the required probability of hazard can be extracted from the graph to represent varying levels of safety around the equipment (Fig. 2). This approach enables the creation of adaptive, elliptical hazard zones whose size, shape, and orientation dynamically respond to the equipment's real-time movement.

$$f(x,y) = \frac{1}{2\pi\sigma_x\sigma_y}\exp\left(-\frac{1}{2}\left[\frac{(x-\mu_x)^2}{{\sigma_x}^2} + \frac{\left(y-\mu_y\right)^2}{{\sigma_y}^2}\right]\right) \quad (1)$$

where x and y represent the longitudinal and lateral displacements from the center of the equipment, and μ_x, μ_y, σ_x and σ_y denote the means and standard deviations along the respective directions. The center of the distribution is taken to coincide with the center of the equipment, and the distribution is assumed to have no correlation between axes (i.e., independent x and y). This assumption is reasonable for construction equipment, which typically operates at relatively low speeds throughout most construction operations.

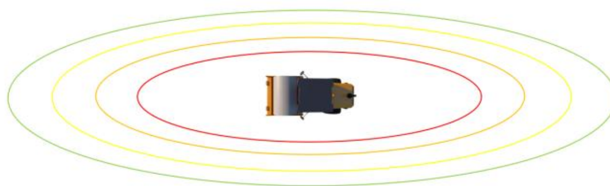

Fig. 2. Elliptical projections from the proposed bivariate Gaussian distribution representing different hazard levels

For a bivariate Gaussian distribution, the elliptical projections are expressed by Eq. 2.

$$\left(\frac{x-\mu_x}{\sigma_x}\right)^2 + \left(\frac{y-\mu_y}{\sigma_y}\right)^2 = k \quad (2)$$

where k is a constant from the chi-squared distribution, representing a specific probability level. The major and minor axes of the ellipse are defined by Eq. 3 and Eq. 4.

$$Major\ axis = 2\sigma_x\sqrt{k} \quad (3)$$

$$Minor\ axis = 2\sigma_y\sqrt{k} \quad (4)$$

The major and minor axes values were expressed as functions of equipment geometry and motion parameters to derive the final hazard zone equation. The formulation of hazard zone dimensions builds upon the procedural framework proposed by Shen et al. [9], where a systematic method for defining safety zones around construction equipment was outlined. In this study, the procedure was adapted and expanded to formulate a dynamic, probabilistic hazard zone aligned with real-time equipment kinematics.

The first consideration was the equipment footprint, characterized by the equipment's length L and width W, which provides the basic dimensions around which the hazard zone must be established. In addition to the physical dimensions, an initial safety boundary S was introduced to ensure a minimum protective margin when the equipment is stationary.

When the equipment is in motion, two dynamic components, operator reaction distance and braking distance, are incorporated to account for real-world stopping behavior. The reaction distance D_R represents the distance traveled during the time taken by the operator to perceive and react to a worker in proximity, as given in Eq. 5.

$$D_R = vt = 2.5v \tag{5}$$

where v is the speed of the equipment, and t is the operator reaction time, taken as 2.5 seconds based on recommendations from prior studies [6], [27]. The braking distance D_B accounts for the distance needed to bring the equipment to a full stop after braking is initiated, as given in Eq. 6.

$$D_B = \frac{v^2}{2a} \tag{6}$$

Using these parameters, the major axis of the elliptical hazard zone, aligned with the heading direction of the equipment, is formulated as the sum of the equipment's physical length, twice the initial safety boundary, and twice the sum of the operator reaction and braking distances (Fig. 3 and Eq. 7).

$$Major\ axis = L + 2S + 2D_R + 2D_B = L + 2S + 5v + \frac{v^2}{a} \tag{7}$$

The minor axis, corresponding to the lateral extent of the hazard zone, is determined as the equipment width plus twice the initial safety boundary (Fig. 3 and Eq. 8).

$$Minor\ axis = W + 2S \tag{8}$$

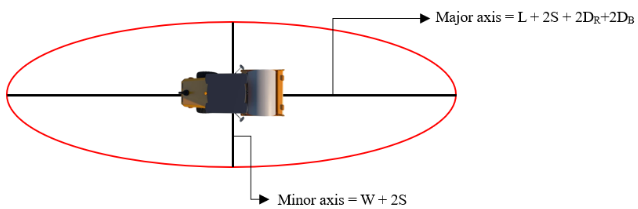

Fig. 3. Major and minor axes of the hazard zone

By equating the geometric formulations for the major and minor axes (Eqs. 7 and 8) with their corresponding probabilistic expressions (Eqs. 3 and 4), explicit relationships for σx and σy as functions of equipment parameters are derived. Specifically, substituting Eq. (7) into Eq. (3) and solving for σx yields Eq. (10), which expresses the longitudinal spread of the distribution as a function of equipment length, safety boundary, speed, and deceleration. Similarly, substituting Eq. (8) into Eq. (4) and solving for σy yields Eq. (12), which depends solely on equipment width and the initial safety boundary, consistent with the assumption that lateral risk extent is independent of equipment motion for translational equipment. With σx and σy established, the constant k in Eq. (2) serves as the remaining degree of freedom: it selects which iso-probability contour of the distribution is treated as the hazard boundary, with larger values of k corresponding to contours farther from the equipment center and enclosing higher cumulative probability mass. The ellipse with a k value of 0.713, corresponding to the 70% hazard level, is selected to represent the primary hazard zone, as it provides a balanced trade-off between early detection and false alarm minimization.

Additional hazard zones representing different risk levels can be generated by varying the k value to establish multi-level warning systems. For example, a caution zone may be defined at k = 0.446, corresponding to the 50% probability level, providing an early advisory boundary at which collision risk begins to rise appreciably, while the primary hazard zone at k = 0.713 marks the boundary at which immediate response is required.

Major axis:

$$2\sigma_x\sqrt{k} = L + 2S + 5v + \frac{v^2}{a} \quad (9)$$

$$\sigma_x = C_1 L + C_2 S + C_3 v + C_4 \frac{v^2}{a} \quad (10)$$

Minor axis:

$$2\sigma_y\sqrt{k} = W + 2S \quad (11)$$

$$\sigma_y = C_5 W + C_6 S \quad (12)$$

where C1 = 0.592, C2 = C6 = 1.183, C3 = 2.959, and C4 = C5 = 0.592 are the coefficients.

As indicated by Eq. (10) and (12), the hazard zone dimension along the major axis adjusts dynamically in response to real-time equipment speed and deceleration rate, while the minor axis dimension remains constant, determined by the equipment's width and initial safety boundary. When the equipment changes heading, the major axis rotates to maintain alignment with the direction of travel.

In practical implementation, high-precision RTK GNSS and IMU sensors continuously track the equipment's position, heading, velocity, and acceleration. These measurements are processed through sensor fusion algorithms to mitigate noise and drift, enabling stable and accurate computation of the kinematic parameters required for real-time hazard zone adjustment according to Eq. (10) and (12). This ensures that the hazard zone remains correctly positioned and oriented relative to the equipment's instantaneous motion state.

Table 1 summarizes the key model parameters and assumptions used throughout the method development. Parameters marked as vehicle-specific, such as equipment length, width, and deceleration, should be obtained from direct measurement or manufacturer specifications, while the initial safety boundary S and the probability-level constant k are configurable and should be set based on site-specific risk tolerance, regulatory requirements, and the acceptable trade-off between false alarms and detection coverage. The operator reaction time t, taken here as 2.5 s based on prior literature, may similarly be adjusted to reflect observed operator characteristics in a given deployment context.

Table 1. Model parameters and assumptions

Symbol	Description	Value / Range	Source / Note
L	Equipment length	Vehicle-specific	Measured
W	Equipment width	Vehicle-specific	Measured
S	Initial safety boundary	1 m used in study	Configurable
t	Operator reaction time	2.5 s	[6, 27]
a	Deceleration during braking	Vehicle-specific	Manufacturer / [10]
k	Probability-level constant for primary hazard boundary	0.713 (70% level)	Configurable

3.2. Hazard zone Dimension Optimization

To refine the hazard zone geometry beyond the initial elliptical formulation, a preliminary simulation study was conducted in Webots software to evaluate the spatial distribution of hazard events around moving equipment [35]. The simulation environment replicated typical highway work zone operating conditions, incorporating GNSS and IMU sensor data with extended Kalman filter-based sensor fusion to track equipment kinematics (Fig. 4). A total of 100 test scenarios were executed, each instantiating one vehicle–worker interaction defined by two independently sampled variables. Equipment speed was drawn from a normal distribution with mean 10 kph and standard deviation 5 kph, truncated to the interval [5, 20] kph to reflect realistic construction equipment operating conditions. Lateral worker position was drawn from a uniform distribution on [−10, +10] m relative to the roadway centerline.

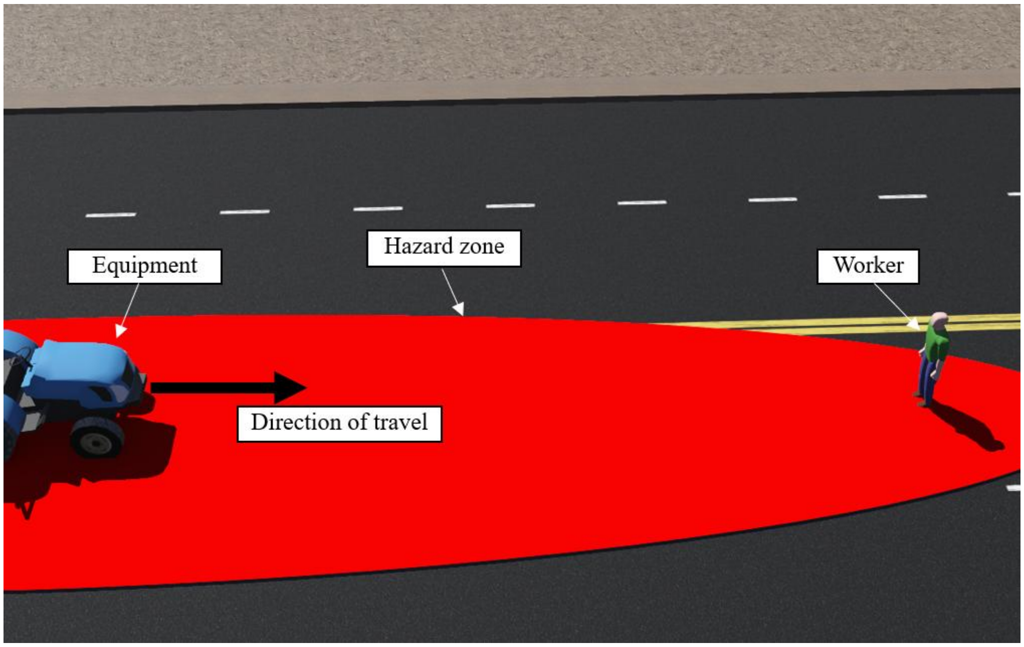

Fig. 4. Webots simulation environment

Analysis of the simulation results revealed that while the elliptical hazard zones derived from the bivariate Gaussian distribution provided substantial improvement over static circular zones, the actual spatial distribution of critical hazard events exhibited a pattern that could be better represented with a superellipse rather than a standard ellipse. Specifically, the hazard zone boundary demonstrated less curvature along the principal axes compared to the theoretical ellipse. This observation suggested that a superelliptical formulation may better capture the observed hazard distribution than a standard elliptical boundary.

To maintain theoretical consistency with the probabilistic framework, the hazard zone formulation was adapted to employ a bivariate generalized Gaussian distribution rather than the standard bivariate Gaussian. The generalized Gaussian extends Eq. (1) by replacing the fixed exponent of 2 in the density function with a free shape parameter p, which controls the curvature of the resulting iso-probability contours. Setting the exponent of this generalized density equal to the threshold constant k, in the same manner that Eq. (2) was derived from Eq. (1), yields the contour equation given in Eq. (13). When $p = 2$, Eq. (13) reduces exactly to Eq. (2), recovering the standard elliptical case. For $p > 2$, the contours transition toward superelliptical geometries with progressively flatter sides and sharper corners, while values of $p < 2$ produce diamond-like shapes with inward-curved sides. The same parameter relationships derived for σ_x and σ_y in Eqs. (10) and (12) remain fully applicable, as these govern the scale of the distribution in the longitudinal and lateral directions regardless of the chosen exponent.

$$\left|\frac{x-\mu_x}{\sigma_x}\right|^p + \left|\frac{y-\mu_y}{\sigma_y}\right|^p = k \quad (13)$$

where p is the superellipse exponent, and k remains the constant corresponding to the desired probability threshold. For p = 2, this reduces to the standard elliptical case; for p > 2, it produces more rectangular geometries with flatter sides and sharper corners; and for p < 2, it yields diamond-like shapes.

To illustrate the geometric evolution induced by the shape parameter, Fig. 5 presents representative contour plots generated from Eq. (13) for values of p equal to 2, 3, 4, 5, and 6. The figure demonstrates the gradual transition from an ellipse to increasingly rectangular superelliptical shapes as p increases.

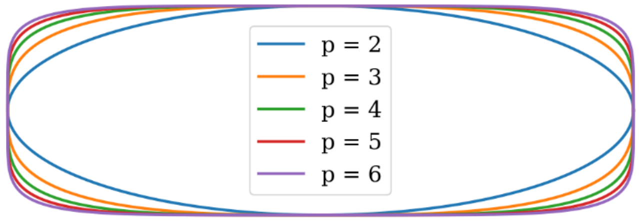

Fig. 5. Evolution of hazard zone geometry with increasing shape parameter p

The selection of the final shape parameter was conducted through comparative simulation analysis. Hazard zone models were implemented using discrete values of p ranging from 2 to 6 in unit increments, and each configuration was evaluated across the simulated scenarios within the same environment. Based on the simulation analysis, a superellipse with p = 4 was found to optimally represent the hazard zone boundaries, providing improved alignment with observed hazard event distributions. The same procedural framework and parameter relationships derived for the standard Gaussian case (Eq. 10 and 12) remain applicable, as the standard deviations σ_x and σ_y continue to govern the scale of the hazard zone in the longitudinal and lateral directions.

4. Experimental Design

With the hazard zone model fully specified, an experimental framework was established to evaluate the proposed dynamic hazard zone model against a conventional static circular approach. The evaluation combined controlled simulation trials and real-world field testing to examine performance under varying operational speeds and interaction scenarios, with emphasis on detection reliability and false alarm behavior.

4.1. Simulation Experiments

The final selected hazard zone model was evaluated through 100 independent simulation runs conducted within the same modeled Webots environment, with equipment speed and worker position sampled from the same distributions and ranges described in Section 3.2. Both the proposed dynamic hazard zone and the static circular baseline were assessed on identical speed and worker position conditions drawn from the same 100 scenarios, ensuring that any performance differences are attributable to the models rather than to variation in input conditions. Each scenario was classified into one of TP, FP, FN, or TN according to the criteria defined in Section 4.3.

4.2. Field Experiments

The field experiment was implemented using an integrated sensing and communication architecture to enable real-time localization and proximity detection during vehicle–worker interactions. The system comprises two main components: an equipment-mounted device and a wearable unit for workers, equipped with u-blox ZED-F9R receivers featuring integrated RTK GNSS and IMU capabilities. These receivers are configured to operate in RTK mode, receiving correction data from a network-based correction service via Networked Transport of RTCM via Internet Protocol (NTRIP). The correction service streams RTK data to the receivers at regular intervals, enabling centimeter-level positioning accuracy. The equipment-mounted device continuously collects location, velocity, and orientation information. These inputs are essential for dynamically updating the parameters of the hazard zone in response to changes in equipment movement.

The wearable unit, positioned on the worker's vest, monitors the worker's location and motion, and is capable of delivering proximity alerts via vibration and audio signals when the worker enters a designated hazard zone. The sensing units also serve as local computation nodes, executing the hazard zone logic onboard to ensure fast, localized response without relying on remote servers.

Communication between devices is handled through a low-power wireless mesh network based on the Thread protocol, which provides robust, scalable, and self-healing connectivity. The implementation uses OpenThread, with equipment-mounted devices acting as routers and worker-worn devices functioning as end devices. The system connects to the external network through a border router that serves as the gateway.

The field experiment was designed to evaluate the real-world effectiveness of the proposed dynamic hazard zone model and compare it with a traditional static circular hazard zone. The experiment involved a vehicle equipped with a sensor device moving toward a worker, while the system continuously monitored whether the worker's location fell within the active hazard zone and issued an alert to the vehicle driver when the worker was detected inside the boundary (Fig. 6). To eliminate safety risks and avoid endangering participants during close vehicle interactions, a mannequin was used in place of a human participant. The mannequin was equipped with the same wearable sensor devices developed for actual workers, enabling accurate location tracking and real-time data transmission to the network. To independently verify whether each alert (or absence of alert) reflected the behavior of the hazard zone model rather than a system or communication failure, the real-time sensor data stream was used to continuously update and visualize the positions of the vehicle, the active hazard zone, and the mannequin, overlaid on a 3D model of the test site using Autodesk Web Viewer (Fig. 6b). This monitoring view was observed in parallel with each trial. Across all the trials reported, no instance of communication loss or alert dropout was observed, and all classified outcomes can therefore be attributed to the hazard zone model itself.

(a) (b)

Fig. 6. Experiment setup (a) physical setup (b) web-based 3D monitoring view

The vehicle followed a fixed straight-line path on a closed test surface for each trial. For each combination of speed and worker position, the vehicle started from a fixed point, accelerated to the target speed of 8.05, 16.1, or 24.14 kph (equivalent to 5, 10, or 15 mph), maintained that speed along the test path, and braked to a stop when an alert was triggered. The vehicle's straight-line path varied slightly between trials due to manual steering, and mannequin placement was adjusted between trials to align the five predefined relative positions (centerline, near-side offset, far-side offset, partially out-of-path, and out-of-path) with the actual line of travel. The trial outcome was determined immediately after each pass, and the vehicle was repositioned for the next trial.

The experimental conditions were structured around two primary hazard zone models: the proposed dynamic hazard zone and a circular static hazard zone, both illustrated in Fig. 7.

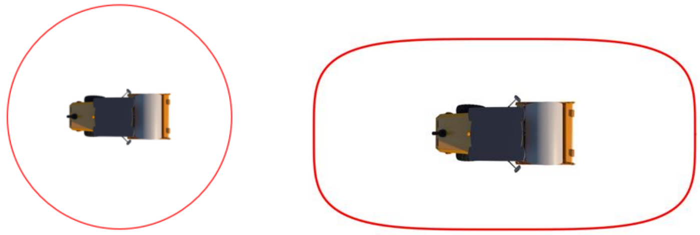

(a) (b)

Fig. 7. Hazard zones (a) circular static hazard zone (b) proposed dynamic hazard zone

Trials were conducted at three speed levels: 8.05 kph (5 mph), 16.1 kph (10 mph), and 24.14 kph (15 mph), and involved 5 predefined worker positions, selected to represent varying proximity and position relative to the vehicle path. The layout of these workers' locations is shown in Fig. 8. Combining these variables resulted in a total of 30 unique trial scenarios (3 speeds × 5 positions × 2 hazard zone models, with one trial per combination).

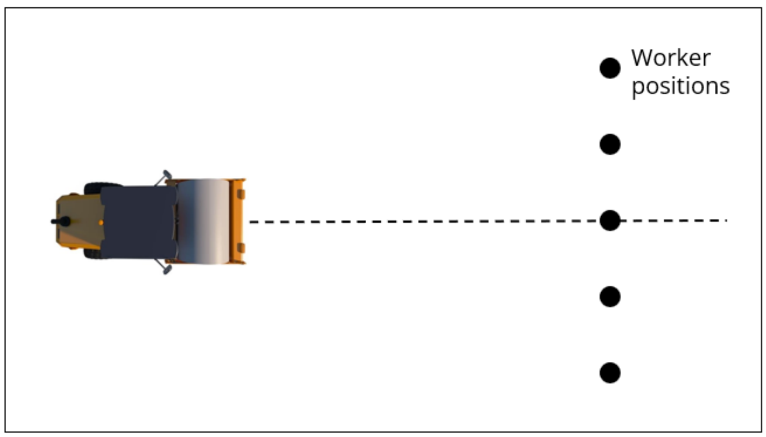

Fig. 8. Layout of worker locations

4.3. Outcome Classification

This section describes how the outcome of each trial was defined and categorized so that the two hazard zone models could be compared consistently. During each trial, the system monitored the proximity between the vehicle and the worker using one of the hazard zone models, and an alert was triggered when the worker was detected within the active hazard boundary. The vehicle operator was instructed to respond to any alert by braking to a complete stop as they naturally would in a real work zone scenario, and the final stopping position relative to the worker was used as the primary basis for outcome classification.

The outcome of each trial was classified into one of four categories based on whether the alert behavior and the vehicle's final stopping position were consistent with safe or unsafe interaction. A True Positive (TP) was recorded when the equipment operator received an alert and brought the vehicle to a safe stop before reaching the worker. A False Positive (FP) corresponded to a trial in which an alert was triggered despite the worker being in a non-threatening location relative to the vehicle path. A False Negative (FN) was recorded when no alert was triggered in time and the vehicle hit or approached the worker dangerously. A True Negative (TN) was recorded when the worker was safely located and correctly did not trigger any alert.

All outcomes were observed and classified in real time by two trained observers, who assessed each scenario based on whether the final stopping position of the vehicle constituted a potential accident or near-miss situation. To supplement these field-based judgments, the positions of the vehicle and the mannequin were continuously logged throughout each trial using the onboard sensors. The recorded position data were used to compute the minimum distance between the vehicle and the mannequin at the point of stopping, providing a quantitative basis for evaluating whether the observed stopping position could be classified as a potential accident, a near-miss, or a safe stop, and thereby supporting the outcome categories assigned by the observers.

4.4. Evaluation Metrics

To evaluate the detection performance of the proposed dynamic hazard zone model, a set of focused classification and distance-based metrics were employed. These metrics were computed based on the trial outcomes categorized into TP, FP, FN, and TN, as defined earlier.

The key metrics used include:

- Accuracy: It represents the proportion of correctly classified trials (Eq. 14).

$$Accuracy = \frac{TP + TN}{TP + TN + FP + FN} \tag{14}$$

- Sensitivity: It quantifies the proportion of actual hazardous situations that are correctly detected (Eq. 15).

$$Sensitivity = \frac{TP}{TP + FN} \tag{15}$$

- False Positive Rate (FPR): It quantifies the proportion of non-hazardous situations that incorrectly triggered an alert (Eq. 16).

$$FPR = \frac{FP}{FP + TN} \tag{16}$$

Both the proposed and the static circular hazard zone models were evaluated across the same set of experimental scenarios and metrics.

5. Results and Discussion

This section presents the results of the pre-field validation experiment conducted in a simulation environment, as well as the field experiment, and provides a comparative discussion of the performance of the proposed dynamic hazard zone model versus the static circular hazard zone. The results subsections report classification outcomes and quantitative performance metrics, while the discussion subsection interprets these findings, explains observed detection errors, and reflects on limitations and broader implications.

5.1. Simulation Experimental Results

A total of 100 simulations were conducted to evaluate the proposed dynamic hazard zone against the conventional static circular hazard zone. Both approaches were assessed using the same classification criteria, and the outcomes are summarized in the confusion matrices shown in Fig. 9. Table 2 presents the raw classification counts alongside accuracy and false positive rate for both models, with 95% Wilson score confidence intervals. The proposed dynamic hazard zone achieved an overall accuracy of 95%, compared to 60% for the static model, and the non-overlapping confidence intervals confirm that this performance difference is systematic rather than a product of sampling variability. To further evaluate statistical significance, McNemar's exact test was applied to the paired binary outcomes across all 100 trials. Given that the dynamic model produced only 5 misclassifications against 40 for the static model, the test yields $p < 0.001$, indicating that the difference in classification performance between the two models is statistically significant. Examining the individual outcome categories, the static circular hazard zone consistently failed to classify true negative situations correctly, generating a false positive rate of 100%. It also failed to detect a notable number of genuinely hazardous situations, producing false negatives that represent the more safety-critical failure mode. In contrast, the dynamic model reduced false positives considerably, achieving an FPR of 5.8%, while correctly identifying the majority of hazardous interactions.

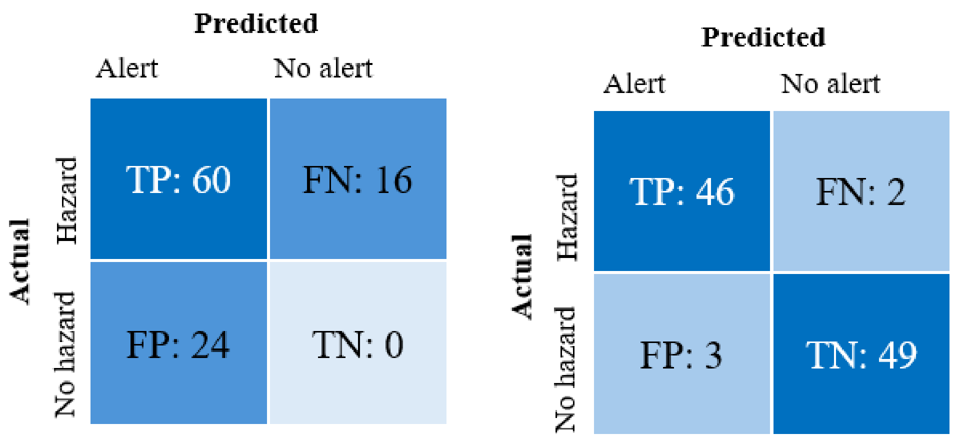

(a) (b)

Fig. 9. Confusion matrices for simulation results (a) static circular hazard zone (b) dynamic hazard zone

Table 2. Simulation experiment classification counts and performance metrics with 95% Wilson score confidence intervals

Model	**TP**	**FP**	**FN**	**TN**	**Accuracy [95% CI]**	**Sensitivity [95% CI]**	**FPR [95% CI]**
Static circular hazard zone	60	24	16	0	60.0% [50.2–69.1%]	78.9% [68.1%, 87.0%]	100% [86.2–100%]
Dynamic hazard zone (proposed)	46	3	2	49	95.0% [88.8–97.8%]	95.8% [85.7%, 98.8%]	5.8% [2.0–15.6%]

To examine the result in more detail, performance was also evaluated across equipment speed ranges. The results are summarized in Table 3. At low speeds, the proposed model maintained near-perfect classification with very few misclassifications, while the static model produced many unnecessary hazard flags. At medium speeds, the proposed model remained stable, whereas the static zone degraded substantially and generated both missed hazards and excessive false alarms. At high speeds, the proposed model showed a modest reduction in accuracy but continued to outperform the static zone by a wide margin, demonstrating better robustness under fast-moving conditions.

Table 3. Breakdown of model performance across different speed ranges

Speed Range	**Hazard Zone**	**TP**	**FP**	**FN**	**TN**	**ACC**
5–10 kph	Proposed	21	1	0	22	97.7%
	Static	37	12	0	0	75.5%
10–15 kph	Proposed	20	1	1	20	95.2%
	Static	17	9	12	0	44.7%

15–20 kph	Proposed	5	1	1	7	85.7%
	Static	6	3	4	0	46.2%

5.2. Field Experimental Results

The field experiment evaluated the real-world performance of the proposed dynamic hazard zone model against a conventional static circular hazard zone, using the same trial protocol and outcome classification scheme. Each trial involved a vehicle equipped with the sensor system moving toward a mannequin representing a worker at predefined speeds. The mannequin was fitted with a wearable sensing unit identical to that designed for actual workers. Fig. 10 illustrates the vehicle trajectories and worker positions plotted on the test map. The mannequin was stationary during each trial but was repositioned between trials to cover the five predefined positions, and the plotted worker positions therefore reflect the logged locations of the mannequin across all trials rather than continuous movement.

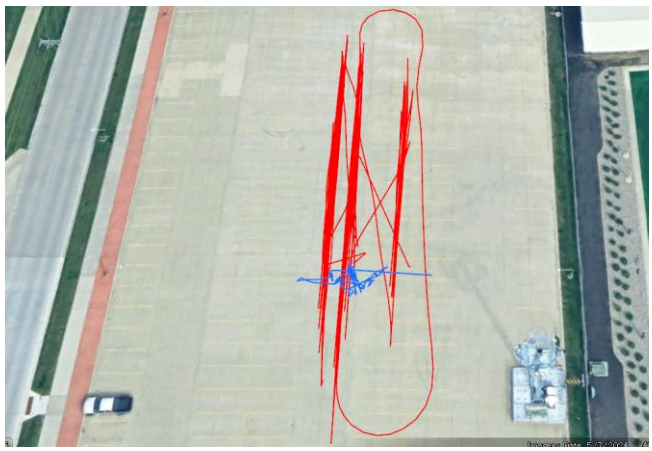

Fig. 10. Vehicle trajectories and worker positions plotted on a map (red: vehicle trajectories; blue: worker positions)

To classify each trial, two complementary evaluation approaches were employed: field observer assessment and distance-based analysis. Two trained observers monitored each test in real time, judging whether the final stopping position of the vehicle constituted a safe stop or a potential near-miss. In parallel, the minimum distance between the vehicle and mannequin was computed from high-precision GNSS coordinates collected during the experiment. This dual validation ensured that both qualitative and quantitative criteria supported the outcome classification.

Trial outcomes were then categorized into four standard groups based on whether an alert was triggered appropriately and whether the vehicle's final stopping position represented a safe stop or a near-miss/unsafe interaction. Aggregate results are summarized in Fig. 11 using confusion matrices for both models.

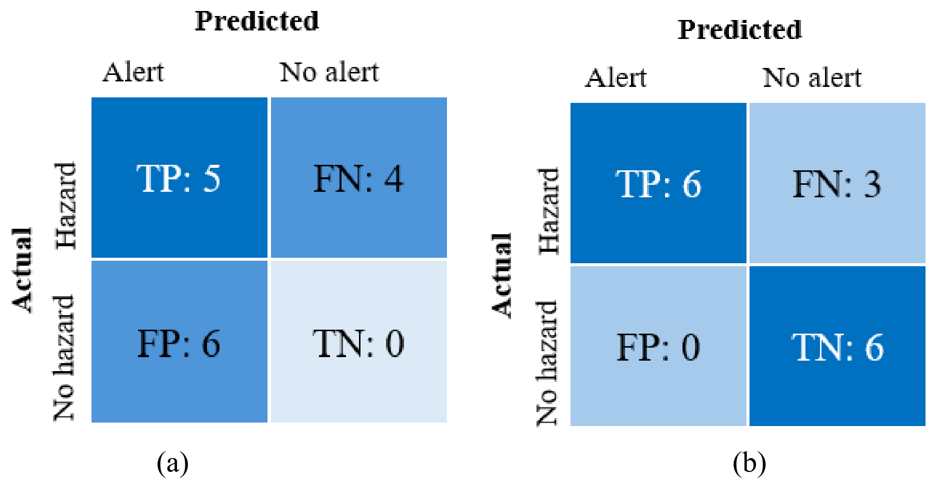

Fig. 11. Confusion matrices for field experiment results (a) static circular hazard zone (b) dynamic hazard zone

In alignment with the simulation findings, the dynamic hazard zone model demonstrated superior detection accuracy and reliability compared to the static circular model. It achieved a higher number of true positives, while substantially reducing both false positives and false negatives. The static model, constrained by its fixed boundary, produced no true negatives, as it frequently encompassed workers who were actually in safe positions. In contrast, the dynamic model accurately distinguished these safe cases, reflecting its adaptive response to real-time equipment motion.

The quantitative metrics in Table 4 reinforce these findings through both point estimates and interval-based analysis. The proposed model achieved an accuracy of 80.0%, compared to 33.3% for the static circular hazard zone, while the reported 95% Wilson score intervals demonstrate a clear separation between the performance of the two models. To evaluate this performance gap, McNemar's exact test was performed, resulting in a p-value of 0.0156 confirming that the dynamic model's superiority is statistically significant ($p < 0.05$) and not attributable to sampling variability. Although accuracy decreased slightly relative to simulation results (as expected under real-world conditions), the decline was minimal for the dynamic model but substantial for the static model. The sensitivity of the dynamic hazard zone reached 66.7%, outperforming the static model's 55.6%. Most notably, the false positive rate (FPR) dropped to 0% for the dynamic model, eliminating all unnecessary alerts that beset the static approach.

In practical terms, each false positive generated by the static model represents an unnecessary alarm triggered while the worker is in a safe position, an outcome that interrupts ongoing operations and progressively erodes operator trust in the system. Conversely, each false negative represents a failure to alert the operator when the worker is genuinely at risk, which is the most safety-critical failure mode a proximity detection system can exhibit. The dynamic model’s substantial reduction in both failure modes relative to the static approach translates directly into a more operationally reliable system under the tested conditions.

Table 4. Field experiment performance metrics with 95% Wilson score confidence intervals

Model	**TP**	**FP**	**FN**	**TN**	**Accuracy [95% CI]**	**Sensitivity [95% CI]**	**FPR [95% CI]**
Static circular hazard zone	5	6	4	0	33.3% [15.2–58.3%]	55.6% [26.7–81.1%]	100% [61.0–100%]
Dynamic	6	0	3	6	80.0%	66.7%	0%

Model	TP	FP	FN	TN	Accuracy [95% CI]	Sensitivity [95% CI]	FPR [95% CI]
hazard zone					[54.8–93.0%]	[35.4–87.9%]	[0–39.0%]

The relationship between detection performance and equipment speed is illustrated in Fig. 12. The plots show that, for the static circular hazard zone (Fig. 12a), both accuracy and sensitivity drop sharply as speed increases, while the false positive rate (FPR) remains consistently high across all speeds. In contrast, the proposed dynamic hazard zone model (Fig. 12b) maintains low false positive rates and sustains moderate, stable accuracy and sensitivity even as speed increases. This demonstrates that the dynamic model effectively adapts to changing motion conditions, providing reliable detection and minimal false alarms across a wide range of operational speeds, whereas the static model's performance rapidly deteriorates under higher-speed conditions.

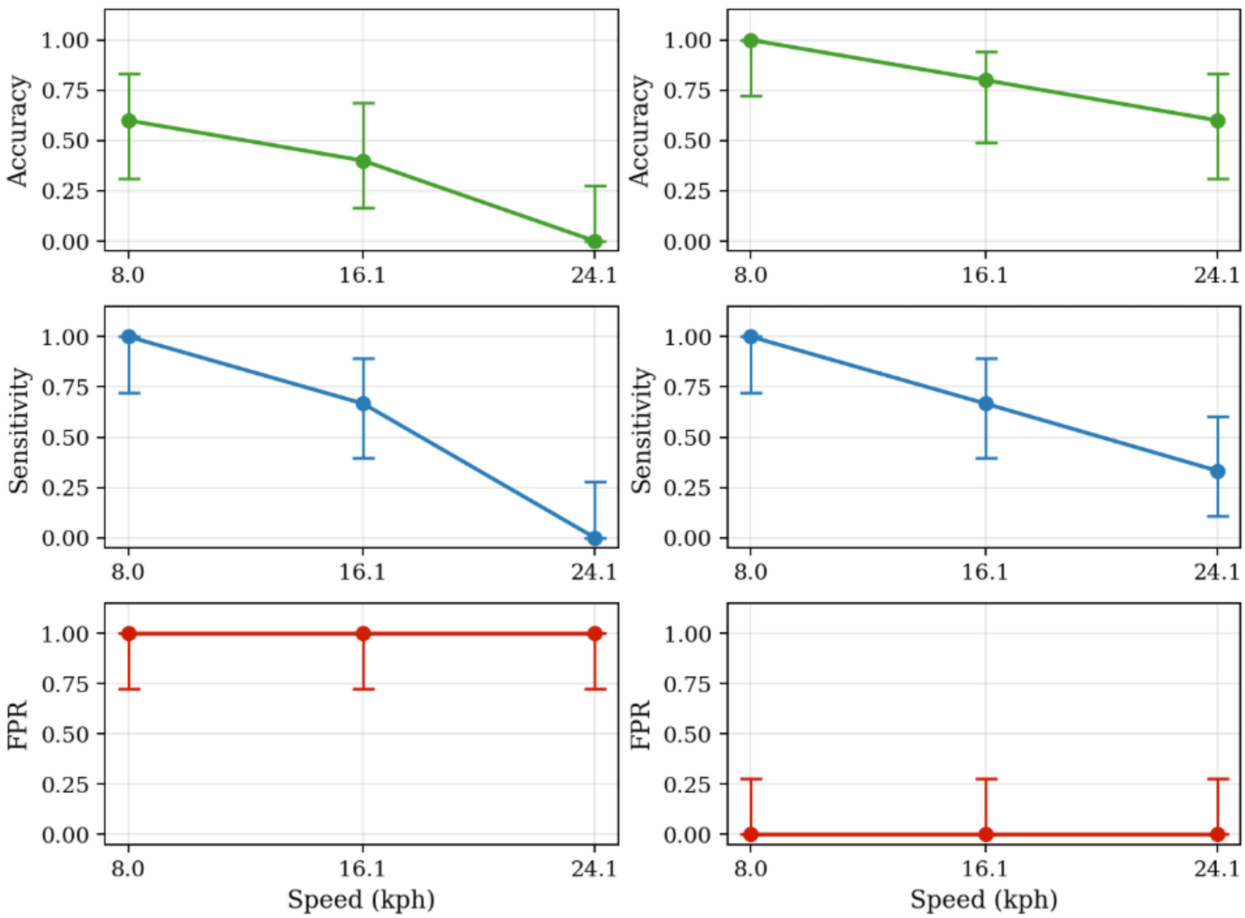

(a) (b)

Fig. 12. Detection performance vs. speed with 95% confidence intervals (a) static circular hazard zone (b) proposed hazard zone

5.3. Discussion

The experimental results indicate that incorporating motion-dependent parameters into hazard zone modeling improves proximity detection performance relative to fixed geometric boundaries. By dynamically adjusting its spatial configuration based on equipment velocity and orientation, the proposed model reduces unnecessary alerts while maintaining reliable hazard detection. This adaptive formulation directly addresses the limitations of conventional proximity systems that rely on static distance thresholds independent of motion context.

From a practical standpoint, the reduction in false positives is particularly significant. Although correctly detecting hazardous situations remains fundamental to any safety system, excessive false alarms can lead to operator desensitization and reduced trust in the system. Across both simulation and field experiments, the dynamic hazard zone consistently produced substantially fewer false positive detections than the static circular model, while maintaining strong hazard detection performance. This balanced improvement in both detection reliability and alert precision indicates greater operational stability under controlled and real-world conditions. Furthermore, the integration of RTK GNSS, IMU sensing, and onboard computation demonstrates that the model operates in real time without reliance on remote cloud infrastructure, supporting responsive deployment in active construction environments where latency and network dependency are critical constraints.

The observed false positives and false negatives across both models reflect distinct failure modes rooted in their underlying formulations. In the static model, false positives arise because the fixed boundary indiscriminately encompasses workers at lateral positions that pose no genuine collision risk, while false negatives at higher speeds occur because the zone does not extend sufficiently in the heading direction to provide adequate warning distance. The modest reduction in proposed-model accuracy at the highest tested speeds is likely attributable to two compounding effects. At higher speeds, the time interval between consecutive sensor updates corresponds to a larger spatial displacement, so any latency in the kinematic state estimate produces a larger error in the inferred position and heading of the equipment. In addition, the hazard zone parameters, particularly σx, which scales with speed and deceleration, change more rapidly with speed, and small lags in updating the boundary therefore translate into proportionally larger boundary-prediction errors when the equipment is moving quickly. Both effects should diminish as sensor sampling and zone-update rates are increased, but they are intrinsic to any system that infers a moving boundary from sampled state and are not specific to the proposed formulation.

While the findings are encouraging, certain limitations should be considered. The field validation was conducted under controlled conditions with a single vehicle type and predefined worker positions, which may not fully represent the variability of complex construction environments. Broader validation across different machinery classes, site geometries, and operational scenarios is necessary to generalize performance claims. Although IMU-based dead reckoning supplements GNSS positioning, localization performance may still degrade in environments affected by GNSS signal obstruction or multipath interference, potentially influencing hazard boundary precision. In addition, the present formulation primarily emphasizes longitudinal motion and does not explicitly account for complex maneuvering behaviors such as sharp turns. The field sample size is small relative to the variability of real construction work zones, and the field findings should therefore be regarded as preliminary evidence rather than definitive performance estimates. The present study compares the proposed model against a static circular baseline, which was selected as the reference because alternative hazard zoning approaches with sufficiently documented implementations for replication under the present experimental conditions remain limited in the literature; evaluation against a broader range of hazard zoning approaches is left to future work.

Future work could extend the framework to incorporate nonlinear trajectory prediction, evaluate performance under signal-degraded environments, extend the formulation to equipment classes with more complex movements, and investigate integration with digital twin platforms for enhanced visualization and predictive safety analysis. Additionally, incorporating more detailed worker motion modeling to account for behavioral variability and pedestrian movement patterns needs to be considered in future work to more fully represent dynamic worker-equipment interactions.

Taken together, the principal strengths of this study lie in three areas. First, the probabilistic formulation grounded in the bivariate generalized Gaussian distribution provides a theoretically coherent basis for representing risk as a continuous spatial field, enabling multi-level hazard boundaries from a single parameterization. Second, the model's direct dependence on real-time RTK GNSS and IMU measurements ensures that hazard zone geometry responds continuously to equipment kinematics rather than relying on assumed or averaged operating parameters. Third, the onboard computation architecture eliminates dependence on remote infrastructure, making the system practically deployable in active construction environments where network connectivity cannot be guaranteed.

6. Conclusion

This paper presented the development and validation of a dynamic probabilistic hazard zone model designed to enhance safety in construction zones by adapting in real time to the motion of construction equipment. Unlike conventional static hazard zones, the proposed model employs a bivariate generalized Gaussian distribution to represent risk as a continuous spatial probability field, enabling the creation of adaptive, multi-level hazard boundaries.

Simulation and field experiments demonstrated that the dynamic model consistently outperformed the static approach in both detection accuracy and operational reliability. In simulation, the model achieved an overall accuracy of 95%, compared to 60% for the static zone, while field tests confirmed significant gains with 80% accuracy and zero false positives. The results further showed that the proposed model maintained stable performance across varying speed ranges, whereas the static model’s accuracy and sensitivity sharply declined with increasing speed.

These findings demonstrate that dynamically adjusting hazard zones based on real-time kinematic data reduces false alarms, improves early hazard detection, and enhances system credibility for work zone safety applications. The findings are based on the evidence from the simulated scenarios and controlled field trials with a single vehicle type and predefined worker positions, and broader validation across additional equipment classes, site geometries, and operating conditions will be necessary to establish the generality of these results. Future work should therefore extend the framework to a wider range of equipment types and real-world site conditions, and investigate its performance under more complex operational scenarios such as sharp turns and irregular trajectories.

Acknowledgment

This material is based upon work supported by the Minnesota Department of Transportation (MNDOT) Grant No. 1036338. Any opinions, findings, and conclusions or recommendations expressed in this material are those of the authors and do not necessarily reflect the view of the MNDOT.

References

[1] J. Hang, X. Li, X. Yan, K. Duan, Q. Wang, Q. Xue, Driving risks assessment and in-vehicle warning design for improving work zone safety, Accid. Anal. Prev. 215 (2025) 107991. https://doi.org/10.1016/J.AAP.2025.107991.

[2] M. Osman, R. Paleti, S. Mishra, Analysis of passenger-car crash injury severity in different work zone configurations, Accid. Anal. Prev. 111 (2018) 161–172. https://doi.org/10.1016/j.aap.2017.11.026.

[3] A.Y. Demeke, M. Younesi Heravi, I.S. Dola, Y. Jang, C. Le, I. Jeong, Z. Lin, D. Wang, Advancing highway work zone safety: A comprehensive review of sensor technologies for intrusion and

proximity hazards, Transp. Res. Rec. (2024). https://doi.org/10.1177/03611981241265845.

[4] J. Teizer, T. Cheng, Proximity hazard indicator for workers-on-foot near miss interactions with construction equipment and geo-referenced hazard areas, Autom. Constr. 60 (2015) 58–73. https://doi.org/10.1016/J.AUTCON.2015.09.003.

[5] O. Golovina, J. Teizer, N. Pradhananga, Heat map generation for predictive safety planning: Preventing struck-by and near miss interactions between workers-on-foot and construction equipment, Autom. Constr. 71 (2016) 99–115. https://doi.org/10.1016/J.AUTCON.2016.03.008.

[6] J. Wang, S.N. Razavi, Low false alarm rate model for unsafe-proximity detection in construction, Journal of Computing in Civil Engineering 30 (2016). https://doi.org/10.1061/(asce)cp.1943-5487.0000470.

[7] B.W. Jo, Y.S. Lee, J.H. Kim, D.K. Kim, P.H. Choi, Proximity warning and excavator control system for prevention of collision accidents, Sustainability 9 (2017) 1488. https://doi.org/10.3390/SU9081488.

[8] X. Luo, H. Li, T. Huang, T. Rose, A field experiment of workers' responses to proximity warnings of static safety hazards on construction sites, Saf. Sci. 84 (2016) 216–224. https://doi.org/10.1016/j.ssci.2015.12.026.

[9] X. Shen, E. Marks, N. Pradhananga, T. Cheng, Hazardous proximity zone design for heavy construction excavation equipment, J. Constr. Eng. Manag. 142 (2016) 05016001. https://doi.org/10.1061/(ASCE)CO.1943-7862.0001108.

[10] J. Park, E. Marks, Y.K. Cho, W. Suryanto, Performance test of wireless technologies for personnel and equipment proximity sensing in work zones, J. Constr. Eng. Manag. 142 (2015) 04015049. https://doi.org/10.1061/(ASCE)CO.1943-7862.0001031.

[11] J. Teizer, Magnetic field proximity detection and alert technology for safe heavy construction equipment operation, in: Proceedings of the 32nd International Symposium on Automation and Robotics in Construction (ISARC 2015), 2015.

[12] J.W. Park, X. Yang, Y.K. Cho, J. Seo, Improving dynamic proximity sensing and processing for smart work-zone safety, Autom. Constr. 84 (2017) 111–120. https://doi.org/10.1016/j.autcon.2017.08.025.

[13] J. Teizer, B.S. Allread, C.E. Fullerton, J. Hinze, Autonomous pro-active real-time construction worker and equipment operator proximity safety alert system, Autom. Constr. 19 (2010) 630–640. https://doi.org/10.1016/j.autcon.2010.02.009.

[14] F. Vahdatikhaki, A. Hammad, Dynamic equipment workspace generation for improving earthwork safety using real-time location system, Advanced Engineering Informatics 29 (2015) 459–471. https://doi.org/10.1016/J.AEI.2015.03.002.

[15] I. Awolusi, E. Marks, N. Pradhananga, T. Cheng, Hazardous proximity zone design for heavy construction equipment, in: 5th International/11th Construction Specialty Conference, 2015. https://doi.org/10.14288/1.0076403.

[16] M. Amiri, A. Ardeshir, M.H. Fazel Zarandi, Fuzzy probabilistic expert system for occupational hazard assessment in construction, Saf. Sci. 93 (2017) 16–28. https://doi.org/10.1016/J.SSCI.2016.11.008.

[17] T.K. Biswas, K. Zaman, A fuzzy-based risk assessment methodology for construction projects under epistemic uncertainty, International Journal of Fuzzy Systems 21 (2019) 1221–1240. https://doi.org/10.1007/S40815-018-00602-W/METRICS.

[18] H. Zhao, S. Li, X. Zang, X. Liu, L. Zhang, J. Ren, Uncertainty quantification of inverse analysis for geomaterials using probabilistic programming, Journal of Rock Mechanics and Geotechnical Engineering 16 (2024) 895–908. https://doi.org/10.1016/J.JRMGE.2023.07.014.

[19] J. Park, Y.K. Cho, A. Khodabandelu, Sensor-based safety performance assessment of individual construction workers, Sensors 18 (2018) 3897. https://doi.org/10.3390/S18113897.

[20] Z. Zhang, W. Li, J. Yang, Analysis of stochastic process to model safety risk in construction industry, Journal of Civil Engineering and Management 27 (2021) 87–99. https://doi.org/10.3846/JCEM.2021.14108.

[21] K.N. Abdrakhmanova, A. V. Fedosov, K.R. Idrisova, N.K. Abdrakhmanov, R.R. Valeeva, Review of modern software complexes and digital twin concept for forecasting emergency situations in oil and gas industry, IOP Conf. Ser. Mater. Sci. Eng. 862 (2020) 032078. https://doi.org/10.1088/1757-899X/862/3/032078.

[22] A. Ochoa-de-Eribe-Landaberea, L. Zamora-Cadenas, I. Velez, Untethered ultra-wideband-based real-time locating system for road-worker safety, Sensors 24 (2024) 2391. https://doi.org/10.3390/S24082391.

[23] W. Umer, M.K. Siddiqui, Use of ultra wide band real-time location system on construction jobsites: Feasibility study and deployment alternatives, International Journal of Environmental Research and Public Health 2020, Vol. 17, Page 2219 17 (2020) 2219. https://doi.org/10.3390/IJERPH17072219.

[24] O. Moselhi, H. Bardareh, Z. Zhu, Automated data acquisition in construction with remote sensing technologies, Applied Sciences 10 (2020) 2846. https://doi.org/10.3390/APP10082846.

[25] N. Soltanmohammadlou, S. Sadeghi, C.K.H. Hon, F. Mokhtarpour-Khanghah, Real-time locating systems and safety in construction sites: A literature review, Saf. Sci. 117 (2019) 229–242. https://doi.org/10.1016/J.SSCI.2019.04.025.

[26] M. Younesi Heravi, A.Y. Demeke, I.S. Dola, Y. Jang, I. Jeong, C. Le, Vehicle intrusion detection in highway work zones using inertial sensors and lightweight deep learning, Autom. Constr. 176 (2025) 106291. https://doi.org/10.1016/j.autcon.2025.106291.

[27] K. Kim, I. Jeong, Y.K. Cho, Signal processing and alert logic evaluation for IoT-based work zone proximity safety system, J. Constr. Eng. Manag. 149 (2023) 05022018. https://doi.org/10.1061/JCEMD4.COENG-12417.

[28] S. Mastrolembo Ventura, P. Bellagente, S. Rinaldi, A. Flammini, A.L.C. Ciribini, Enhancing safety on construction sites: A UWB-based proximity warning system ensuring GDPR compliance to prevent collision hazards, Sensors 23 (2023) 9770. https://doi.org/10.3390/S23249770.

[29] J. Teizer, H. Neve, H. Li, S. Wandahl, J. König, B. Ochner, M. König, J. Lerche, Construction resource efficiency improvement by long range wide area network tracking and monitoring, Autom. Constr. 116 (2020) 103245. https://doi.org/10.1016/J.AUTCON.2020.103245.

[30] M. Younesi Heravi, I.S. Dola, Y. Jang, I. Jeong, Edge AI-enabled road fixture monitoring system, Buildings 14 (2024) 1220. https://doi.org/10.3390/BUILDINGS14051220.

[31] I. Jeong, Y. Jang, I. Sharmin Dola, M. Younesi Heravi, A framework for remote road furniture monitoring system using smart IoT dashcams and digital twin, Computing in Civil Engineering (2024) 1080–1088. https://doi.org/10.1061/9780784485248.129.

[32] Y. Liu, H. Wang, Z. Cai, D. Chen, K. Han, Enabling high-fidelity and real-time mobility digital twin with edge computing, in: Proceedings - 2022 IEEE/ACM 7th Symposium on Edge Computing, SEC 2022, Institute of Electrical and Electronics Engineers Inc., 2022: pp. 281–283. https://doi.org/10.1109/SEC54971.2022.00031.

[33] T. Cao, Y. Wang, S. Liu, Pavement crack detection based on 3D edge representation and data communication with digital twins, IEEE Transactions on Intelligent Transportation Systems 24 (2023) 7697–7706. https://doi.org/10.1109/TITS.2022.3194013.

[34] Y. Gao, S. Qian, Z. Li, P. Wang, F. Wang, Q. He, Digital twin and its application in transportation infrastructure, in: Proceedings 2021 IEEE 1st International Conference on Digital Twins and Parallel Intelligence, DTPI 2021, Institute of Electrical and Electronics Engineers Inc., 2021: pp. 298–301. https://doi.org/10.1109/DTPI52967.2021.9540108.

[35] Cyberbotics Ltd., Cyberbotics: Robotics simulation with Webots, Cyberbotics (n.d.). https://cyberbotics.com/ (accessed February 19, 2026).